



Title	Formation and field-assisted dissolution of anodic films on iron in fluoride-containing organic electrolyte
Author(s)	Shahzad, Khurram; Tsuji, Etsushi; Aoki, Yoshitaka; Nagata, Shinji; Habazaki, Hiroki
Citation	Electrochimica acta, 151, 363-369 <a href="https://doi.org/10.1016/j.electacta.2014.10.132">https://doi.org/10.1016/j.electacta.2014.10.132</a>
Issue Date	2015-01-01
Doc URL	<a href="http://hdl.handle.net/2115/57952">http://hdl.handle.net/2115/57952</a>
Type	article (author version)
File Information	E_field_EA_rev.pdf



[Instructions for use](#)

**Formation and field-assisted dissolution of anodic films on iron in fluoride-containing  
organic electrolyte**

Khurram Shahzad<sup>a</sup>, Etsushi Tsuji<sup>a,b</sup>, Yoshitaka Aoki<sup>a,b</sup>, Shinji Nagata<sup>c</sup>,  
and Hiroki Habazaki<sup>a,b,1,\*</sup>

<sup>a</sup> Graduate School of Chemical Sciences and Engineering, Hokkaido University, Sapporo,  
Hokkaido 060-8628, Japan

<sup>b</sup> Division of Materials Chemistry & Frontier Chemistry Center, Faculty of Engineering,  
Hokkaido University, Sapporo, Hokkaido 060-8628, Japan

<sup>c</sup> Institute for Materials Research, Tohoku University, 2-1-1, Katahira, Aoba-ku, Sendai  
980-8577, Japan

\*Corresponding author: habazaki@eng.hokudai.ac.jp, TEL & FAX: +81-11-706-6575

<sup>1</sup> ISE member

**Abstract:**

Magnetron-sputtered iron films were potentiodynamically anodized at two different sweep rates to 50 V in an ethylene glycol electrolyte containing ammonium fluoride and water. At a high sweep rate of  $1.0 \text{ V s}^{-1}$ , a barrier-type anodic film was formed even though the current efficiency was as low as ~50%. In contrast, a nanoporous anodic film developed at a low sweep rate of  $0.05 \text{ V s}^{-1}$ , and the film-formation efficiency reduced to 37%. The main part of the anodic films consists of iron (III) hydroxyfluoride with a thin inner layer composed of  $\text{FeF}_3$ . The inner fluoride layer is formed owing to the faster inward migration of fluoride ions compared to that of the oxygen species. During immersion or re-anodizing of the iron specimen with an approximately 100-nm-thick, barrier-type anodic film at and below 15 V, thinning of the anodic film proceeded uniformly and film dissolution was enhanced by applying an electric field. The impact of the electric field on film formation and dissolution is discussed.

**Keywords:** Anodizing, iron, porous anodic film, organic electrolyte, fluoride

## 1. Introduction

Nanoporous oxide films, formed by anodizing valve metals such as Al, Ti, Zr, Nb, Ta, and W, have been extensively explored in the last two decades because of their practical importance as well as of fundamental interest in the growth mechanism. These films have potential applications in corrosion protection, nanodevices, solar cells, batteries, and templates for the fabrication of various nanomaterials [1-4]. There are three types of anodic films: barrier-type, nanoporous-type, and nanotubular-type. Their formation depends upon the anodizing conditions, such as the anodizing electrolyte and anodizing voltage/current. The barrier-type anodic films are typically formed when growth proceeds at a high current efficiency. When the films are amorphous, new film materials are developed both at the film/electrolyte and metal/film interfaces by outward migration of cations and inward migration of anions, respectively, in a correlative manner [5].

The formation behavior of self-organized porous oxide films has attracted much attention in recent years. It is well accepted that porous anodic films are formed when new film material is formed only at the metal/film interface, while cation species migrating outwards are ejected directly to the electrolyte at the film/electrolyte interface [6]. Most recent studies have focused on the understanding of the mechanism of pore generation, and efforts have been made to resolve the causes of field-induced and stress-induced instabilities at the

film/electrolyte interface, which leads to pore formation [7-10]. It is generally presumed that pores initiate at a rough film/electrolyte interface under an electric field, where the field is non-uniformly concentrated at the troughs of the film/electrolyte interface. Various mechanisms have been proposed for the growth of porous oxides over the past 50 years, namely (a) field-induced dissolution, (b) field-assisted ejection, and (c) field-assisted plastic flow [6, 8, 11, 12]. In the field assisted dissolution model, first proposed by Hoar and Mott [13], it is presumed that the generation of pores is associated with the dynamic equilibrium between the rate of oxide formation at the metal/film interface and the dissolution of the oxide at the film/electrolyte interface. Most investigations in the field-assisted dissolution model assume that steady-state film growth kinetics occur due to an accelerating dissolution of the oxide film under the influence of a high external electric field at the pore base [6, 11, 13, 14].

Recently, Garcia et al. proposed that the generation and growth of a porous anodic structure on aluminum is associated with the field-assisted flow of oxide material by a distribution of compressive stresses [12, 15-18]. Through a series of tracer experiments, they concluded that pores are generated by plastic flow of material from the pore base towards the cell walls in certain electrolytes. In parallel, Hebert and co-workers support their flow model using a computational approach [8, 19].

In both field-assisted dissolution and field-assisted flow models, the electric field applied in the barrier layer sandwiched between the porous layer and metal substrate plays a crucial role. Direct experimental evidences of the influence of the electric field on dissolution and pore initiation and the presence of a critical field for pore initiation during the anodizing of aluminum have been demonstrated recently by Oh and Thomson [9]. They showed that uniform thinning of the oxide film occurs below a field of  $7.46 \text{ MV cm}^{-1}$ , and field-induced instability and pore initiation start at this critical field. The mechanical instability that leads to major pore formation begins at  $8.9 \text{ MV cm}^{-1}$ .

As mentioned above, porous anodic films can be formed on a range of metals. Fluoride-containing organic electrolytes with a small amount of water have been often used for the formation of porous anodic films on titanium [20], zirconium [21], niobium [22], and iron [23-27]. The nanoporous and nanotubular anodic films formed on iron have attracted attention due to their future promising applications, including photoanodes for water splitting, electrodes for lithium ion batteries, gas sensors, and electrodes for electrochemical capacitors [27-32]. Photoelectrochemical characterization of as-anodized and thermally treated anodic films on iron was also carried out in details [33]. Despite extensive investigations on the mechanism of porous film formation on aluminum, studies on the formation mechanism of porous anodic films on iron have been very limited [23-25].

In the present study, we first formed barrier-type and nanoporous-type anodic films on iron by potentiodynamic anodizing in an ethylene glycol electrolyte containing ammonium fluoride and water, and their formation behavior was examined. Then, the influence of an electric field on dissolution rate of anodic films on iron was investigated by applying an electric field to the pre-formed barrier-type anodic film in order to elucidate the crucial role of the electric field in anodizing iron.

## 2. Experimental

Iron thin films of  $\sim 460$  nm thickness were prepared by DC magnetron sputtering. The target was a 99.9% pure iron disk of 0.5 mm thickness and 100 mm diameter bonded on a copper backing plate. Glass plates and electropolished, anodized aluminum sheets were used as the substrate. The latter substrates were used for Rutherford backscattering spectroscopy (RBS) analysis.

The iron thin films were potentiodynamically anodized at varying sweep rates (1.0 and  $0.05 \text{ V s}^{-1}$ ) in a two-electrode cell with a platinum sheet as the counter electrode. The electrolyte was ethylene glycol (EG) containing  $0.1 \text{ mol L}^{-1}$  ammonium fluoride and  $0.1 \text{ mol L}^{-1}$  water at 273 K. After anodizing, the specimens were washed in EG and then in acetone. The relatively low temperature and low water concentration in the electrolyte was selected to

reduce the chemical dissolution rate and to promote the formation of a barrier –type film to higher formation voltages.

The surfaces and cross-sections of the anodized iron specimens were observed using a JEOL JSM-6500F field emission scanning electron microscope operated at an accelerating voltage of 10 kV. The composition of the anodic films were determined by RBS using a  $\text{He}^{2+}$  ion beam of 2.0 MeV energy supplied by a tandem-type accelerator at Tohoku University. The RBS data were analyzed using the RUMP program [34].

### 3. Results and Discussion

#### 3.1. Potentiodynamic growth of anodic films

Magnetron-sputtered iron films were potentiodynamically anodized to 50 V at 1.0 and  $0.05 \text{ V s}^{-1}$  in the EG electrolyte containing  $0.1 \text{ mol L}^{-1} \text{ NH}_4\text{F}$  and  $0.1 \text{ mol L}^{-1} \text{ H}_2\text{O}$  at 273 K. The typical current-voltage responses are shown in Fig. 1. Initially, the current density increases almost linearly to a current peak, followed by a current decrease to a steady-state current density. At the potential sweep rate of  $0.05 \text{ V s}^{-1}$ , a second small current peak appears at 12 V, in addition to the first higher current peak at 4 V. Assuming that uniform thickening of the anodic film occurs, the growth of the barrier anodic film can be described by the following equation,



$$\frac{dV}{dt} = E \frac{dh}{dt} \quad (1)$$

where  $V$  is the applied voltage,  $t$  is the anodizing time,  $E$  is the electric field across the anodic film, and  $h$  is the thickness of the anodic film. Considering Faraday's law, the following equation can be described,

$$\frac{dV}{dt} = \frac{\eta EM i}{zF} \quad (2)$$

where  $\eta$  is the current efficiency for film growth,  $M$  is the molar volume,  $i$  is the anodizing current,  $z$  is the equivalent number, and  $F$  is Faraday's constant. This equation suggests that under a constant potential sweep rate ( $dV/dt = \text{constant}$ ), current becomes constant under a steady state condition, as in the case of Fig. 1. The presence of the current peak at a low voltage region during potentiodynamic anodizing has been found often in the anodizing of valve metals. The phenomenon was well discussed in a review paper by Lorengel [35] and explained in terms of a delayed oxide formation.

Although there are only limited studies on anodic film growth under potentiodynamic conditions [36-38], Curioni et al. potentiodynamically anodized high purity aluminum in a sulfuric acid electrolyte [36]. In contrast to the observation of a steady-state current in the present study, they found a continuous current increase above a narrow plateau potential region less than 3 V. This was interpreted by the flow model, which was valid in anodizing aluminum in sulfuric acid [7, 39]. Because of the flow of film material, part of the

anodic oxide generated at the metal/film interface is displaced to the cell walls. The displacement tends to reduce the thickness of the barrier layer, contributing to an increase in the electric field and current density. Even though a porous film is formed at the low potential sweep rate as indicated below, the absence of such a continuous current increase in the present study may suggest that the flow model is not applicable here.

Fig. 2 shows the scanning electron micrographs of surfaces of the magnetron-sputtered iron films as-deposited and anodized to 50 V at 0.05 and 1.0 V s<sup>-1</sup>. Associated with the columnar structure of the as-deposited film, a relatively rough surface is observed in Fig. 2a. The apparent grain size (column width) is 50–100 nm. Similar surface morphology is observed after anodizing to 50 V at 1.0 V s<sup>-1</sup> (Fig. 2b), with troughs along the grain boundaries; however, the surface appears to be smoother within grains. For the iron film anodized at the low sweep rate (Fig. 2c), nanopores develop with an average pore size of ~10 nm. The nanopores are formed preferentially at the trough region of the rough surface. Similar results were reported previously in the anodizing of carbon steel [40] as well as aluminum [2]. This means that the site of pore initiation can be controlled by texturing of the metal surface prior to anodizing of iron.

The formation of a barrier-type anodic film at the high sweep rate of 1.0 V s<sup>-1</sup> is confirmed from the scanning electron micrograph of a cross-section of the anodized iron

specimen (Fig. 3a). On the columnar iron layer, a compact anodic film of  $100 \pm 5$  nm thickness developed. The metal/film interface is relatively flat, while the film/electrolyte interface is rough, though barrier-type films formed at high current efficiency typically have a flat film/electrolyte interface. A similar rough film/electrolyte interface and/or a thin porous layer above a barrier layer was found when aluminum was potentiodynamically anodized to 40 V in a tartaric acid electrolyte; no film material was formed at the film/electrolyte interface due to direct ejection of outwardly migrating  $\text{Al}^{3+}$  ions [41]. As discussed later, no film material is formed at the film/electrolyte interface because of the low current efficiency in the formation of the present barrier-type anodic film on iron. In the anodic film formed at the low sweep rate, cylindrical nanopore channels are developed (Fig. 3b). The thickness of the anodic film is  $400 \pm 7$  nm and the barrier layer, sandwiched between the porous layer and iron substrate, has a thickness of  $72 \pm 5$  nm, which is slightly thinner than that formed at the high sweep rate. The interpore distance is  $\sim 60$  nm. When anodizing aluminum in acid electrolytes, the interpore distance is controlled by the formation voltage ( $2.5\text{--}2.8 \text{ nm V}^{-1}$ ) [14]. Since the thickness of the barrier layer beneath the porous alumina layer is  $\sim 1.0 \text{ nm V}^{-1}$ , the interpore distance of the porous layer for porous anodic alumina is 2.5–2.8 times the thickness of the barrier layer. Compared with the morphology of the porous alumina films, the interpore distance in the porous film on iron is too small with respect to the thickness of the barrier layer. The interpore distance of the anodic film on iron appears to be similar to the column

width of the deposited iron. Considering the preferential formation of pores at the trough region of the as-deposited iron surface, it is likely that the interpore distance is controlled by the morphology of the iron surface, not the anodizing parameters under the present anodizing condition. Field-assisted dissolution, rather than field-assisted flow, appears to be dominant in growing porous films on iron under the present conditions.

The composition of the anodic films formed on iron was examined by RBS. Fig. 4 shows the experimental and simulated RBS spectra of the as-deposited iron films and anodized to 50 V at the sweep rates of 1.0 and 0.05 V s<sup>-1</sup>. The RBS spectrum of the as-deposited iron (Fig. 4a) shows yields from iron, aluminum, and oxygen, with the latter two arising from the anodized aluminum substrate. In Fig. 4b, yields from fluorine and oxygen in the anodic film appear separately from the other yields, and a higher yield of fluorine in comparison with oxygen indicates that the anodic film is fluoride-rich. In Fig. 4c, the yield from oxygen appears again, but the yield from fluorine is overlapped with that from iron. The precise composition of the anodic films was examined by simulation. The simulated spectra, shown in Figs. 4b and 4c, obtained using the composition, density, and thicknesses of individual layers in Table 1, are fit with the respective experimental spectra. In the simulation, probable incorporation of carbon species derived from EG into the anodic films was neglected due to a low RBS sensitivity for carbon. The anodic film formed at the high sweep rate

196 consists of two layers: the outer layer (composed of iron (III) hydroxyfluoride or hydrated  
197 oxyfluoride) and the inner layer (composed of iron (III) fluoride). The formation of the inner  
198 fluoride layer may be associated with the faster inward migration of fluoride ions compared  
199 with oxygen species, as reported previously [25]. The faster migration of fluoride in growing  
200 barrier-type anodic films has also been reported in the anodizing of tantalum [42] and  
201 titanium [43]. The outer layer of the present barrier-type anodic film is composed of hydrated  
202 oxide or contains hydroxide. Since the anodic film formed under the present condition is  
203 soluble in water, there is a possibility that the hydration proceeded in laboratory air after  
204 anodizing, not during anodizing.

205         The porous anodic film formed at the low sweep rate also has a compositionally  
206 layered structure. The porous layer, 328 nm thick, is composed of hydrated hydroxyfluoride  
207 and a barrier layer of 72 nm thickness. Both layers have a composition similar to the  
208 respective layers formed at the high sweep rate.

209         From the comparison, determined by the RBS spectra of as-deposited iron films  
210 anodized to 50 V, the thicknesses consumed by anodizing were  $40 \pm 3$  and  $75 \pm 3$  nm at the  
211 high and low sweep rates, respectively. Assuming that iron was oxidized to the Fe (III) state,  
212 the respective electric charges required to oxidize iron were  $0.16 \pm 0.02$  and  $0.31 \pm 0.02$  C  
213  $\text{cm}^{-2}$ , as shown in Table 2. The electric charges passed during anodizing to 50 V at the high

214 and low sweep rates were  $0.15 \pm 0.01$  and  $0.57 \pm 0.02 \text{ C cm}^{-2}$ , respectively. It is obvious from  
215 these results that the electric charge passed during anodizing is used predominantly for the  
216 oxidation of iron at the high sweep rate, while it reduces to 54% at the low sweep rate. During  
217 anodizing at the low sweep rate, gas generation was observed, to a minor extent, from the  
218 specimen surface, contributing to the reduction of the efficiency of iron oxidation. The likely  
219 presence of gas bubbles in the barrier layer may also contribute to the reduction of the barrier  
220 layer thickness ( $\sim 72 \text{ nm}$ ) in comparison with that at the high sweep rate. The electric charge  
221 used for the formation of anodic films was also calculated from the number of iron (III) ions  
222 in the anodic films and the current efficiency for film formation was then estimated (Table 2).  
223 Although a barrier-type film is formed at the high sweep rate, the current efficiency is only  
224 49%. It is likely that film materials are formed only at the metal/film interface by inward  
225 migration of anions and the direct ejection of outwardly migrating cation species occurs at the  
226 film/electrolyte interface; the latter contributes to the reduced efficiency of film formation. At  
227 the low sweep rate, the current efficiency is further reduced to 37%, but 68% of the oxidized  
228 iron was converted to the anodic film. The increased conversion efficiency during porous film  
229 growth at the low sweep rate, compared with that for the barrier film growth at the high sweep  
230 rate, is of interest, being related to the field-assisted dissolution process and/or the probable  
231 presence of oxygen gas bubbles in the barrier layer formed at the low sweep rate. Thus, the  
232 field-assisted dissolution was examined in detail.

233

### 234 3.2. Field-assisted dissolution

235 In order to examine the influence of an electric field on the dissolution of anodic  
236 films formed on iron, a barrier-type film of 100 nm thickness was first formed by anodizing  
237 the magnetron-sputtered iron film to 50 V at the high sweep rate of  $1.0 \text{ V s}^{-1}$ . Then, several  
238 constant voltages were applied to the anodized specimen and the change in the film thickness  
239 was examined. Fig. 5 shows the change in the current density during the re-anodizing of the  
240 iron/anodic film (100 nm) specimen, at 10, 15, 20, and 30 V. The current density is initially  
241 very low at 10 V, since the pre-formed anodic film was developed to 50 V and the initial field  
242 strength is too low for ion migration. However, the current density gradually increases with  
243 time. The initial, very low, current is also found at 15 V, but the current increase occurs from  
244 the commencement of re-anodizing when 20 and 30V is applied.

245 Fig. 6 shows scanning electron micrographs of cross-sections before and after  
246 re-anodizing at several voltages for 1000 s. It is obvious that the anodic film of approximately  
247 100 nm thickness (Fig. 6a) shows a uniform thickness reduction to 76 nm after re-anodizing at  
248 10 V for 1000 s (Fig. 6b). A further reduced thickness to 67 nm is observed at 15 V (Fig. 6c),  
249 indicating that an electric field-assisted dissolution occurs. During re-anodizing at these  
250 voltages, the morphology of the anodic films does not change; no porous film is developed. In

251 contrast, thickening of the anodic film takes place at 20 V (Fig. 6d). Although the pores are  
252 not clearly seen in the anodic film at the available SEM resolution, a porous film must be  
253 grown for film thickening at 20 V. Thickening of the porous film was clearly observed after  
254 re-anodizing at 30 V (Fig. 6e).

255           The change in the anodic film thickness during immersion and re-anodizing at 10  
256 and 15 V (Fig. 7a) shows an accelerated dissolution under an applied electric field. During  
257 immersion of the pre-anodized specimen, film thinning occurs at a rate of  $0.47 \text{ nm min}^{-1}$ . The  
258 dissolution rate is enhanced by applying 10 and 15 V, with the latter voltage resulting in a  
259 more enhanced dissolution rate. Since the thickness reduction occurs during re-anodizing, the  
260 electric field across the barrier layer changes. The change in the electric field with  
261 re-anodizing time is shown in Fig. 7b. Since the field-assisted dissolution is found at 10 V and  
262 a re-anodizing time of 600 s, an electric field of  $1.2 \text{ MV cm}^{-1}$  appears to be sufficient to  
263 enhance the dissolution of the anodic film on iron. This electric field is much lower than that  
264 for anodic alumina ( $5.5 \text{ MV cm}^{-1}$ ), as examined by Oh and Thompson [9]. Oh and Thompson  
265 also reported the presence of a critical field ( $7.46 \text{ MV cm}^{-1}$ ) for pore initiation due to  
266 field-induced instability. In the anodic film on iron, the critical field must be higher than  $2.8$   
267  $\text{MV cm}^{-1}$ , since no pores were found when the electric field was increased to this value at 15  
268 V (Fig. 7b).



269 In summary, anodizing iron in a fluoride-containing EG electrolyte, the electric field  
270 has a crucial role in the dissolution and morphology of the anodic films, as with aluminum in  
271 acid electrolytes. Major pores formed by the mechanical instability (flow of film materials),  
272 found in the anodizing of aluminum, were not formed under the present anodizing condition  
273 for iron. Thus, pores formed due to field-assisted dissolution appear to be dominant in the  
274 anodizing of iron.

275

#### 276 4. Conclusions

277 Anodic films are formed on magnetron-sputtered iron films by potentiodynamic anodizing  
278 to 50 V at two different sweep rates of 1.0 and 0.05 V s<sup>-1</sup> in an EG electrolyte containing 0.1  
279 mol L<sup>-1</sup> NH<sub>4</sub>F and 0.1 mol L<sup>-1</sup> H<sub>2</sub>O at 273K. The film morphology is dependent upon the  
280 sweep rate: a barrier-type at the high sweep rate and a nanoporous-type at the low sweep rate.  
281 The barrier-type film is formed even at a low current efficiency of 49%, suggesting no film  
282 material develops at the film/electrolyte interface. In contrast, a nanoporous anodic film  
283 develops by anodizing to the same 50 V at the low sweep rate of 0.05 V s<sup>-1</sup>. Pores are  
284 developed preferentially along with the surface troughs, which corresponds to the boundaries  
285 of the columnar morphology. The anodic films compositionally consist of an outer iron (III)

hydroxyfluoride layer and an inner FeF<sub>3</sub> layer; the latter layer forming because of the faster migration of fluoride ions in comparison with that of the oxygen species.

When an electric field is applied to the barrier-type anodic film formed by sweeping to 50 V at the high sweep rate, chemical dissolution at the film/electrolyte interface is accelerated. The field-assisted dissolution is also of importance in anodizing iron to form nanoporous anodic films. No evidence of plastic flow from the pore base to the cell walls is found under the present anodizing conditions.

#### Acknowledgments

This work was supported in part by the "Nanotechnology Platform" program of the Ministry of Education, Culture, Sports, Science and Technology (MEXT), Japan.

#### References

- [1] C. Blawert, W. Dietzel, E. Ghali, G.L. Song, Adv. Eng. Mater., 8 (2006) 511-533.
- [2] H. Masuda, K. Fukuda, Science, 268 (1995) 1466-1468.
- [3] T. Kyotani, L.-f. Tsai, A. Tomita, Chem. Mater., 7 (1995) 1427-1428.
- [4] P. Roy, S. Berger, P. Schmuki, Angew. Chem., Int. Ed., 50 (2011) 2904-2939.
- [5] L. Young, D.J. Smith, J. Electrochem.Soc., 126 (1979) 765-768.

304 [6] G.E. Thompson, *Thin Solid Films*, 297 (1997) 192-201.

305 [7] S.J. Garcia-Vergara, L. Iglesias-Rubianes, C.E. Blanco-Pinzon, P. Skeldon, G.E.

306 Thompson, P. Campestrini, *Proceedings of the Royal Society A: Mathematical, Physical*

307 *and Engineering Sciences*, 462 (2006) 2345-2358.

308 [8] J.E. Houser, K.R. Hebert, *Nat. Mater.*, 8 (2009) 415-420.

309 [9] J. Oh, C.V. Thompson, *Electrochim. Acta*, 56 (2011) 4044-4051.

310 [10] K.R. Hebert, S.P. Albu, I. Paramasivam, P. Schmuki, *Nat. Mater.*, 11 (2012) 162-166.

311 [11] G.E. Thompson, R.C. Furneaux, G.C. Wood, J.A. Richardson, J.S. Goode, *Nature*, 272

312 (1978) 433-435.

313 [12] S.J. Garcia-Vergara, P. Skeldon, G.E. Thompson, H. Habazaki, *Electrochim. Acta*, 52

314 (2006) 681-687.

315 [13] T.P. Hoar, N.F. Mott, *J. Phys. Chem. Solids*, 9 (1959) 97-99.

316 [14] J.P. O'Sullivan, G.C. Wood, *Proc. R. Soc. London, A*, 317 (1970) 511-543.

317 [15] F. Zhou, A. Baron-Wiecheć, S.J. Garcia-Vergara, M. Curioni, H. Habazaki, P.

318 Skeldon, G.E. Thompson, *Electrochim. Acta*, 59 (2012) 186-195.

319 [16] F. Zhou, A.K.M. Al-Zenati, A. Baron-Wiechec, M. Curioni, S.J. Garcia-Vergara, H.

320 Habazaki, P. Skeldon, G.E. Thompson, *J. Electrochem. Soc.*, 158 (2011) C202-C214.

321 [17] S.J. Garcia-Vergara, D. Le Clere, T. Hashimoto, H. Habazaki, R. Skeldon, G.E.

322 Thompson, *Electrochim. Acta*, 54 (2009) 6403-6411.

323 [18] S.J. Garcia-Vergara, P. Skeldon, G.E. Thompson, H. Habazaki, *Thin Solid Films*, 515  
324 (2007) 5418-5423.

325 [19] J.E. Houser, K.R. Hebert, *Phys. Status Solidi A*, 205 (2008) 2396-2399.

326 [20] J.M. Macak, P. Schmuki, *Electrochim. Acta*, 52 (2006) 1258-1264.

327 [21] S. Berger, J. Faltenbacher, S. Bauer, P. Schmuki, *Physica Status Solidi-Rapid*  
328 *Research Letters*, 2 (2008) 102-104.

329 [22] W. Wei, K. Lee, S. Shaw, P. Schmuki, *Chem. Commun.*, 48 (2012) 4244-4246.

330 [23] A. Jagminas, K. Mazeika, N. Bernotas, V. Klimas, A. Selskis, D. Baltrunas, *Appl.*  
331 *Surf. Sci.*, 257 (2011) 3893-3897.

332 [24] A. Jagminas, V. Klimas, K. Mazeika, N. Bernotas, A. Selskis, G. Niaura, *Electrochim.*  
333 *Acta*, 56 (2011) 5452-5458.

334 [25] H. Habazaki, Y. Konno, Y. Aoki, P. Skeldon, G.E. Thompson, *J. Phys. Chem. C*, 114  
335 (2010) 18853-18859.

336 [26] S.P. Albu, A. Ghicov, P. Schmuki, *Physica Status Solidi-Rapid Research Letters*, 3  
337 (2009) 64-66.

338 [27] H.E. Prakasam, O.K. Varghese, M. Paulose, G.K. Mor, C.A. Grimes, *Nanotechnol.*, 17  
339 (2006) 4285-4291.

340 [28] S.K. Mohapatra, S.E. John, S. Banerjee, M. Misra, *Chem. Mater.*, 21 (2009)  
341 3048-3055.

342 [29] R.R. Rangaraju, A. Panday, K.S. Raja, M. Misra, J. Phys. D: Appl. Phys., 42 (2009)  
343 135303.

344 [30] Z.H. Zhang, M.F. Hossain, T. Takahashi, Appl. Cat. B-Env., 95 (2010) 423-429.

345 [31] K.Y. Xie, J. Li, Y.Q. Lai, W. Lu, Z.A. Zhang, Y.X. Liu, L.M. Zhou, H.T. Huang,  
346 Electrochem. Commun., 13 (2011) 657-660.

347 [32] H. Cheng, Z.G. Lu, R.G. Ma, Y.C. Dong, H.E. Wang, L.J. Xi, L.X. Zheng, C.K. Tsang,  
348 H. Li, C.Y. Chung, J.A. Zapien, Y.Y. Li, J. Mater. Chem., 22 (2012) 22692-22698.

349 [33] M. Santamaria, S. Terracina, Y. Konno, H. Habazaki, F. Di Quarto, J. Solid State  
350 Electrochem., 17 (2013) 3005-3014.

351 [34] L.R. Doolittle, Nucl. Instr. and Meth., B9 (1985) 344-351.

352 [35] M.M. Lohrengel, Mater. Sci. Eng. R-Rep., 11 (1993) 243-294.

353 [36] M. Curioni, P. Skeldon, G.E. Thompson, J. Electrochem. Soc., 156 (2009) C407.

354 [37] F. Di Franco, G. Zampardi, M. Santamaria, F. Di Quarto, H. Habazaki, J.  
355 Electrochem. Soc., 159 (2012) C33-C39.

356 [38] M. Santamaria, F. Di Quarto, S. Zanna, P. Marcus, Electrochim. Acta, 56 (2011)  
357 10533-10542.

358 [39] S.J. Garcia-Vergara, P. Skeldon, G.E. Thompson, H. Habakaki, Corros. Sci., 49  
359 (2007) 3696-3704.

360 [40] Y. Konno, S. Yang, E. Tsuji, Y. Aoki, P. Skeldon, G.E. Thompson, H. Habazaki, ECS  
361 Trans., 50 (2013) 183-190.

362 [41] M. Curioni, T. Gionfini, A. Vicenzo, P. Skeldon, G.E. Thompson, Surf. Interface Anal.,  
363 45 (2013) 1485-1489.

364 [42] K. Shimizu, K. Kobayashi, G.E. Thompson, P. Skeldon, G.C. Wood, J. Electrochem.  
365 Soc., 144 (1997) 418-423.

366 [43] H. Habazaki, K. Fushimi, K. Shimizu, P. Skeldon, G.E. Thompson, Electrochem.  
367 Commun., 9 (2007) 1222-1227.

368

369

370 Figure captions

371 Fig. 1  $I$ - $V$  responses of magnetron-sputtered iron films at potential sweep rates of 0.05 and  
372  $1.0 \text{ V s}^{-1}$  in an EG electrolyte containing  $0.1 \text{ mol L}^{-1} \text{ NH}_4\text{F}$  and  $0.1 \text{ mol L}^{-1} \text{ H}_2\text{O}$  at 273 K.

373

374 Fig. 2 Scanning electron micrographs of surfaces of the magnetron-sputtered iron films (a)  
375 as-deposited and anodized to 50 V at sweep rates of (b) 1.0 and (c)  $0.05 \text{ V s}^{-1}$  in an EG  
376 electrolyte containing  $0.1 \text{ mol L}^{-1} \text{ NH}_4\text{F}$  and  $0.1 \text{ mol L}^{-1} \text{ H}_2\text{O}$  at 273 K.

377

378 Fig. 3 Scanning electron micrographs of cross-sections of the magnetron-sputtered iron  
379 films anodized to 50 V at sweep rates of (a) 1.0 and (b)  $0.05 \text{ V s}^{-1}$  in an EG electrolyte  
380 containing  $0.1 \text{ mol L}^{-1} \text{ NH}_4\text{F}$  and  $0.1 \text{ mol L}^{-1} \text{ H}_2\text{O}$  at 273 K.

381

382 Fig. 4 Experimental and simulated RBS spectra of magnetron-sputtered iron films (a)  
383 as-deposited and anodized to 50 V at sweep rates of (b) 1.0 and (c)  $0.05 \text{ V s}^{-1}$  in an EG  
384 electrolyte containing  $0.1 \text{ mol L}^{-1} \text{ NH}_4\text{F}$  and  $0.1 \text{ mol L}^{-1} \text{ H}_2\text{O}$  at 273 K.

385

Fig. 5 Current transients of magnetron-sputtered iron films with a pre-formed 100-nm-thick, barrier-type anodic film during re-anodizing at several constant voltages in an EG electrolyte containing 0.1 mol L<sup>-1</sup> NH<sub>4</sub>F and 0.1 mol L<sup>-1</sup> H<sub>2</sub>O at 273 K.

Fig. 6 Scanning electron micrographs of cross-sections of magnetron-sputtered iron films with a pre-formed 100-nm-thick, barrier-type anodic film (a) before anodizing, and after re-anodizing at (b) 10 V for 1000 s, (c) 15 V for 1000 s, (d) 20 V for 1000 s, and (e) 30 V for 1000 s in an EG electrolyte containing 0.1 mol L<sup>-1</sup> NH<sub>4</sub>F and 0.1 mol L<sup>-1</sup> H<sub>2</sub>O at 273 K.

Fig. 7 (a) Change in thickness of the pre-formed 100-nm-thick anodic films during immersion and re-anodizing at 10 and 15 V in an EG electrolyte containing 0.1 mol L<sup>-1</sup> NH<sub>4</sub>F and 0.1 mol L<sup>-1</sup> H<sub>2</sub>O at 273 K and (b) the respective change in the electric field associated with the thinning of the anodic films.



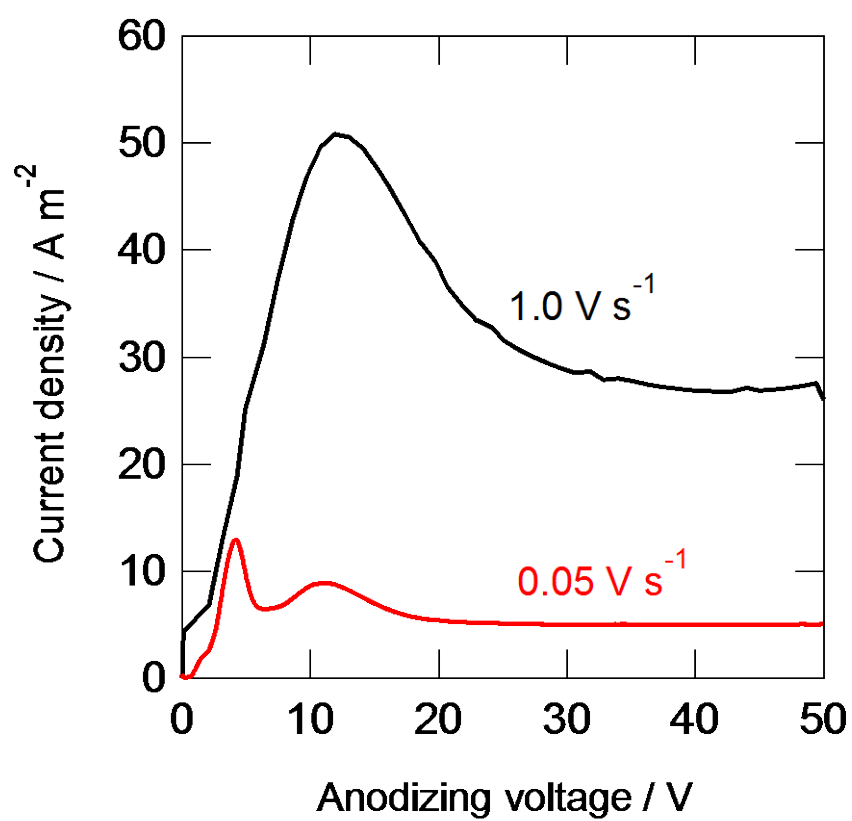


Figure 1.

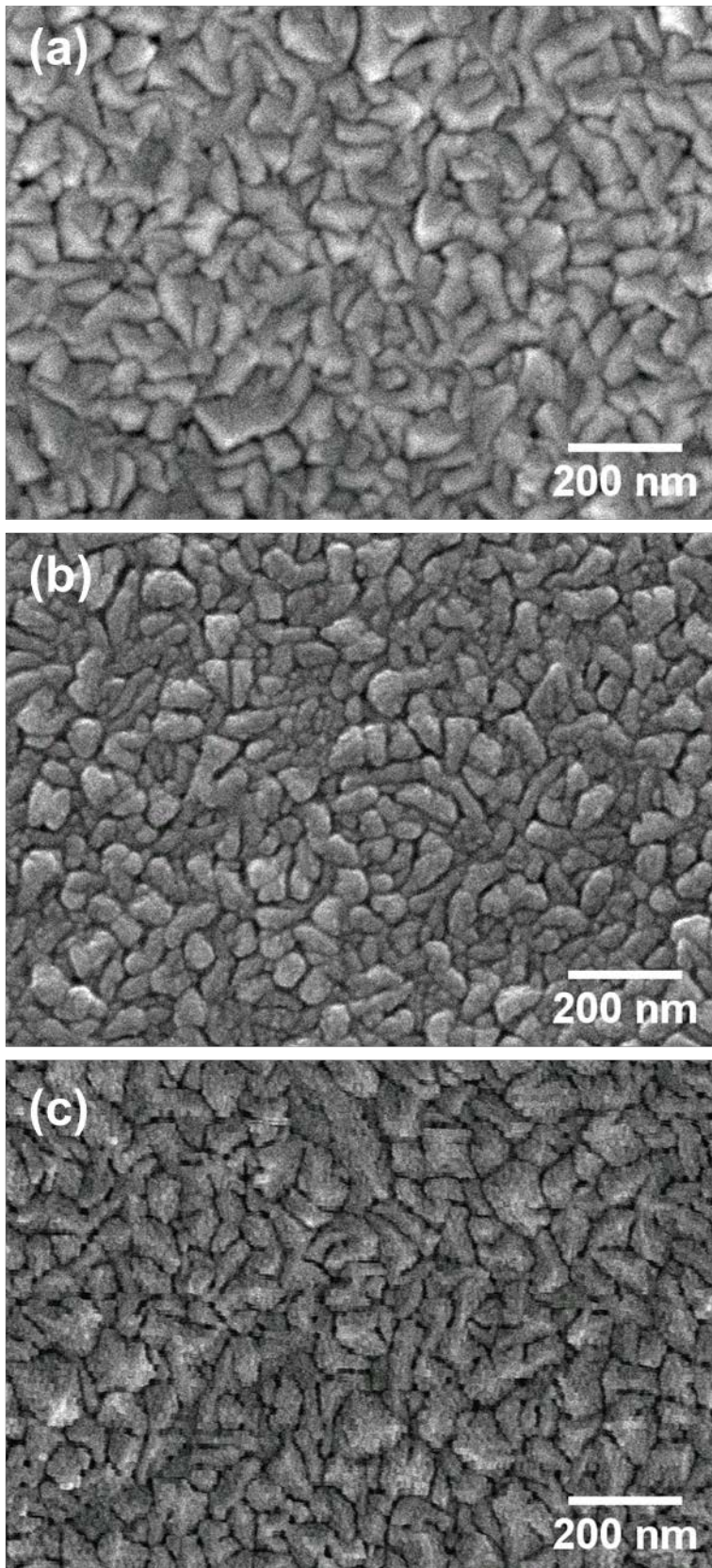


Fig. 2

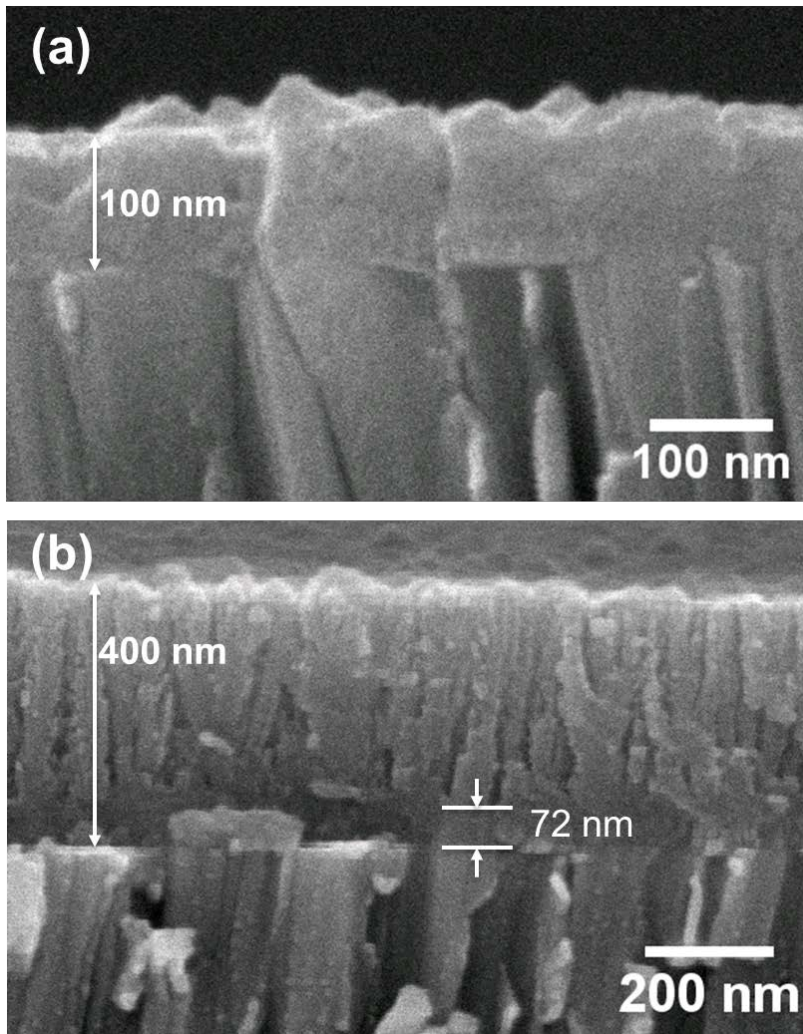


Fig. 3

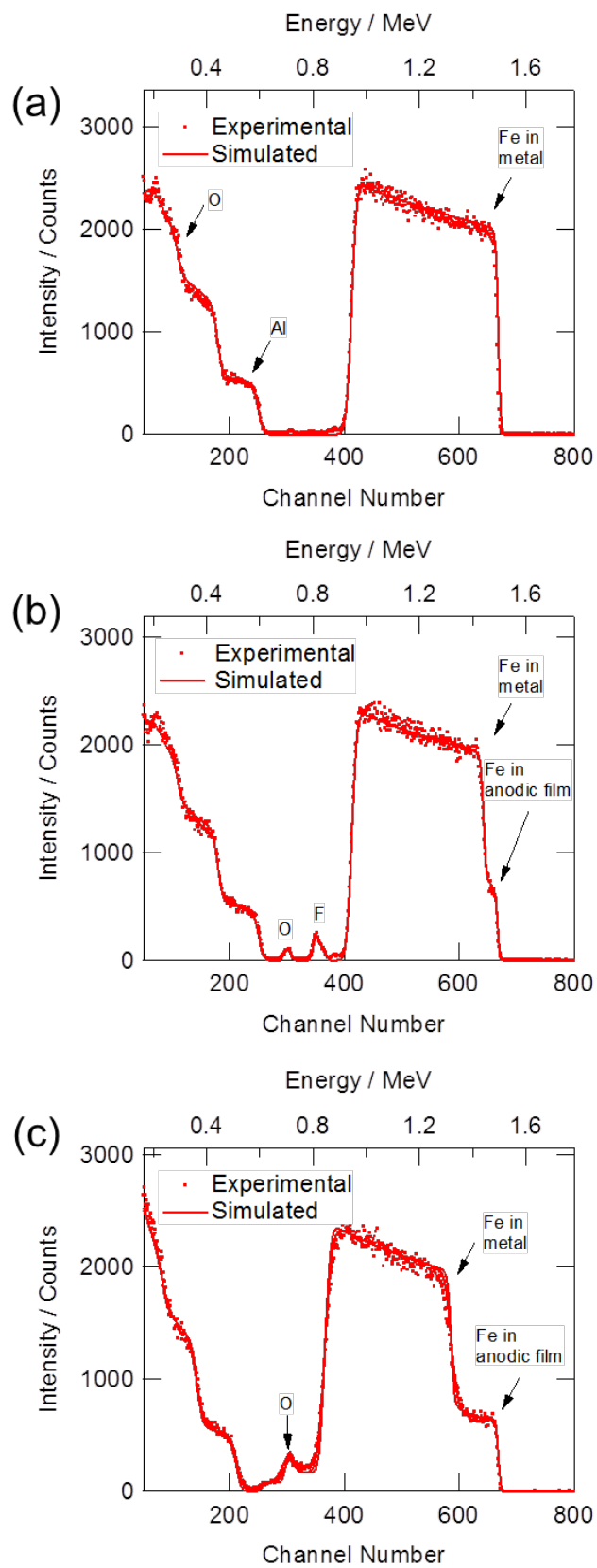


Fig. 4

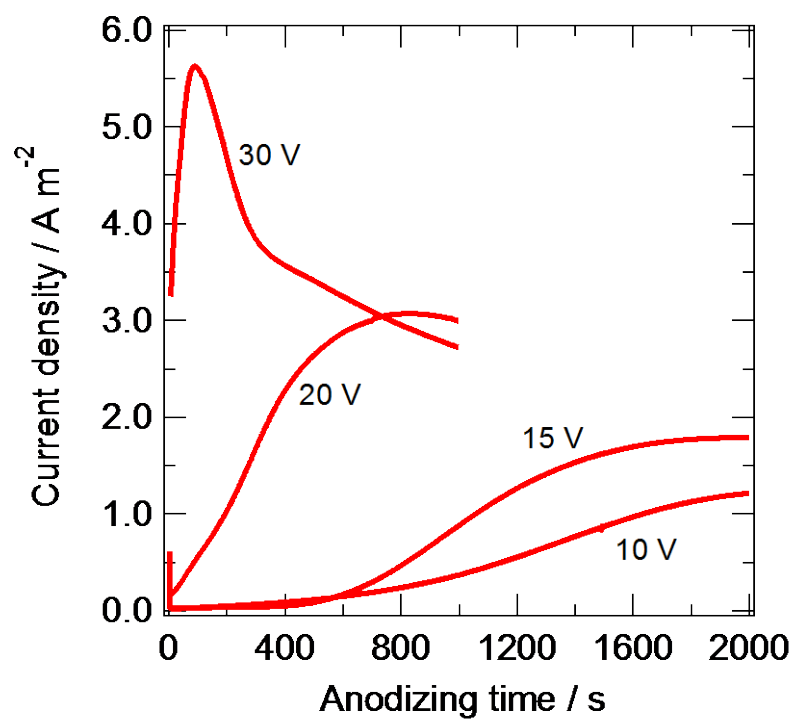


Fig. 5

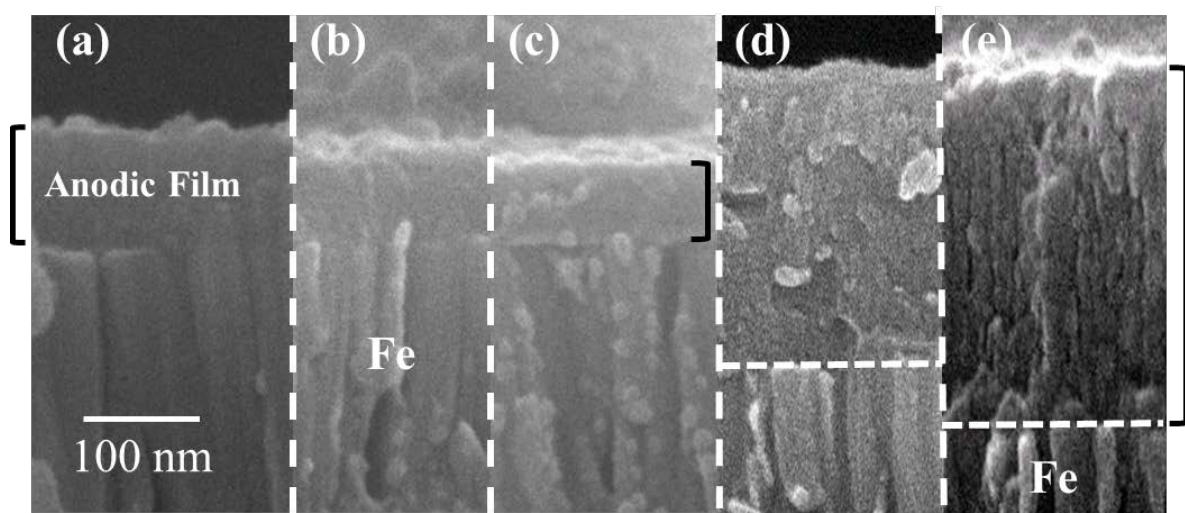


Fig. 6

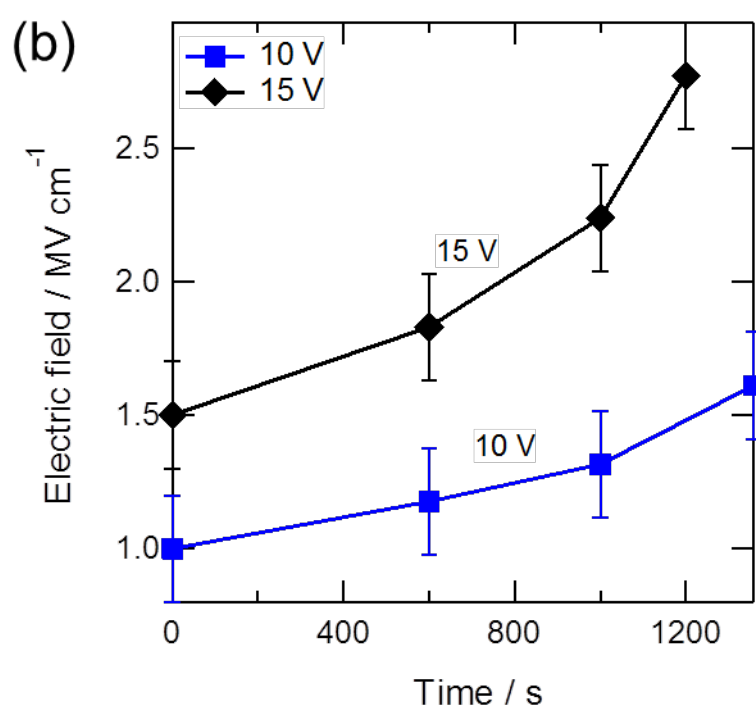
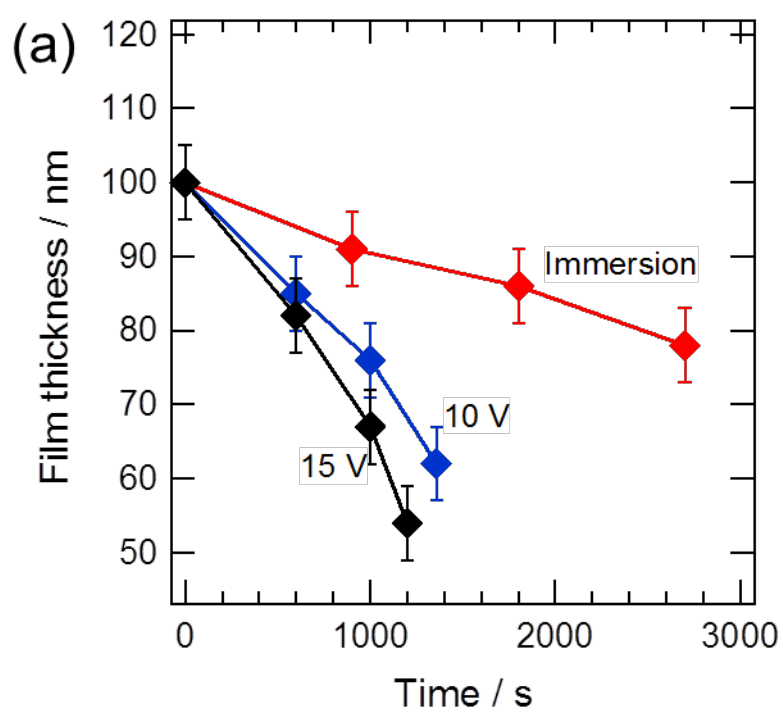


Fig. 7